Title

The 4D Camera: An 87 kHz Direct Electron Detector for Scanning/Transmission Electron Microscopy

Permalink

https://escholarship.org/uc/item/7fs8w6m8

Journal

Microscopy and Microanalysis, 30(5)

ISSN

1431-9276

Authors

Ercius, Peter

Johnson, Ian J

Pelz, Philipp

et al.

Publication Date

2024-09-19

DOI

10.1093/mam/ozae086

Copyright Information

Peer reviewed

The 4D Camera: An 87 kHz Direct Electron Detector for Scanning/Transmission Electron Microscopy

Peter Ercius, Ian J Johnson, Philipp Pelz, Benjamin H Savitzky, Lauren Hughes, Hamish G Brown, Steven E Zeltmann, Shang-Lin Hsu, Cassio C S Pedroso, Bruce E Cohen, Ramamoorthy Ramesh, David Paul, John M Joseph, Thorsten Stezelberger, Cory Czarnik, Matthew Lent, Erin Fong, Jim Ciston, Mary C Scott, Colin Ophus, Andrew M Minor, Peter Denes

The 4D Camera: An 87 kHz Direct Electron Detector for Scanning/Transmission Electron Microscopy

Peter Ercius[1,*] , Ian J. Johnson[2], Philipp Pelz[1], Benjamin H. Savitzky[1], Lauren Hughes[1], Hamish G. Brown[1], Steven E. Zeltmann[3], Shang-Lin Hsu[3], Cassio C.S. Pedroso[4], Bruce E. Cohen[4,5], Ramamoorthy Ramesh[3,6,7], David Paul[8], John M. Joseph[2], Thorsten Stezelberger[2], Cory Czarnik[9], Matthew Lent[9], Erin Fong[2], Jim Ciston[1], Mary C. Scott[1,3], Colin Ophus[1], Andrew M. Minor[1,3], and Peter Denes[1]

[1]National Center for Electron Microscopy, Molecular Foundry, Lawrence Berkeley National Laboratory, Berkeley, CA 94720, USA
[2]Division of Engineering, Lawrence Berkeley National Laboratory, Berkeley, CA 94720, USA
[3]Department of Materials Science and Engineering, University of California Berkeley, Berkeley, CA 94720, USA
[4]Molecular Foundry, Lawrence Berkeley National Laboratory, Berkeley, CA 94720, USA
[5]Division of Molecular Biophysics and Integrated Bioimaging, Lawrence Berkeley National Laboratory, Berkeley, CA 94720, USA
[6]Division of Materials Science, Lawrence Berkeley National Laboratory, Berkeley, CA 94720, USA
[7]Department of Physics, University of California Berkeley, Berkeley, CA 94720, USA
[8]National Energy Research Scientific Computing Center, Lawrence Berkeley National Laboratory, Berkeley, CA 94720, USA
[9]Gatan Inc., Pleasanton, CA 94588, USA
*Corresponding author: Peter Ercius, E-mail: percius@lbl.gov

Abstract

We describe the development, operation, and application of the 4D Camera—a 576 by 576 pixel active pixel sensor for scanning/transmission electron microscopy which operates at 87,000 Hz. The detector generates data at ~480 Gbit/s which is captured by dedicated receiver computers with a parallelized software infrastructure that has been implemented to process the resulting 10–700 Gigabyte-sized raw datasets. The back illuminated detector provides the ability to detect single electron events at accelerating voltages from 30 to 300 kV. Through electron counting, the resulting sparse data sets are reduced in size by 10–300× compared to the raw data, and open-source sparsity-based processing algorithms offer rapid data analysis. The high frame rate allows for large and complex scanning diffraction experiments to be accomplished with typical scanning transmission electron microscopy scanning parameters.

Key words: active pixel sensor, direct electron detector, phase contrast STEM, scanning transmission electron microscopy, 4D-STEM

Introduction

Progress in direct electron detectors (DEDs) for transmission electron microscopy (TEM) has recently lead to significant advances in almost every aspect of the field (MacLaren et al., 2020). DEDs provide significantly faster readout, zero dead time (rolling shutter readout), and large improvements in sensitivity compared to traditional charge-coupled device (CCD) cameras. DEDs avoid the conversion process of electrons-to-photons-to-electrons involved in the use of CCDs with a scintillator. This leads to improvements in sensitivity, point spread function (PSF), and detector quantum efficiency (DQE). DEDs have achieved great success in solving three-dimensional (3D) biological structures (such as proteins) in the field of cryogenic electron microscopy due to their improved sensitivity (to reduce dose) (McMullan et al., 2009) and speed (to correct motion blur) (Brilot et al., 2012; Grob et al., 2013). Further, *in situ* TEM has greatly benefited from the improved time resolution (~1 ms) and use of "rolling readout" mode to eliminate the duty cycle (dead 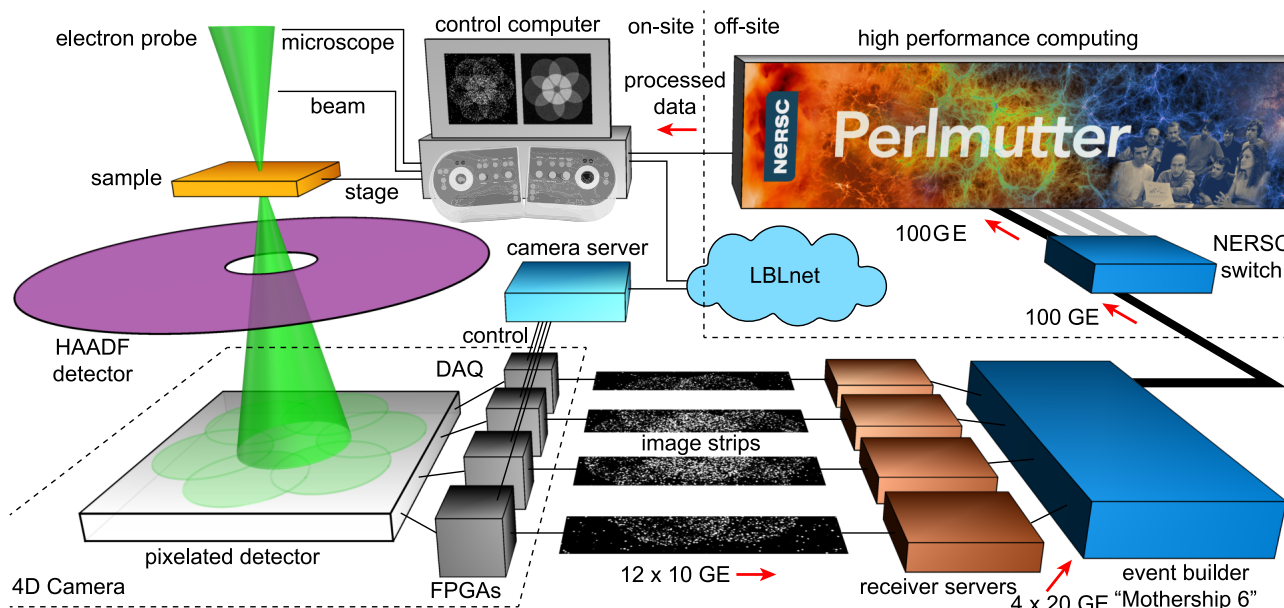time) of older detector technologies allowing every electron to contribute to the measurement (Park et al., 2015; Kim et al., 2020). DEDs are also incorporated into spectrometers for electron energy loss spectroscopy (EELS) and scanning electron microscopes for electron backscatter diffraction with great success (Hart et al., 2017; Susarla et al., 2022).

The application of advanced DEDs for scanning TEM (STEM) allows the user to acquire a two-dimensional (2D) convergent beam electron diffraction (CBED) pattern at every scan position in a 2D set of scanning positions. The resulting data set is thus four-dimensional (4D) leading to the common term of 4D-STEM (Ophus, 2019). This is a rapidly evolving field enabling the acquisition of data with traditional STEM image contrast produced by radial, monolithic detectors as well as enabling new imaging modalities (Nord et al., 2020; Paterson et al., 2020). For example, ptychography has achieved extremely high resolutions (Chen et al., 2021) and the ability to image high- and low-scattering elements simultaneously (Yang et al., 2017). Reconstruction of the 3D scattering potential is possible by so-called S-matrix Reconstruction from a focal series of

Fig. 1. A schematic of the 4D Camera detector, data acquisition, and data processing system. Each 1/4 sector of the detector is separately processed by four FPGAs and forwarded to four receiver servers. The receiver servers buffer the data in main memory at the full data rate until a scan is complete. Data are then offloaded to the event builder PC (named "Mothership 6") which includes a fast connection to the NERSC supercomputer system. Data can be locally or remotely processed for rapid feedback at the microscope.

4D-STEM datasets (Brown et al., 2018, 2022). Electric field measurements have been shown possible at the atomic level (Hachtel et al., 2018; Murthy et al., 2021). Strain and structural measurements at the atomic- to nano-scale are possible due to scanned (near-) parallel beam techniques (Hirata et al., 2011; Ozdol et al., 2015; Zeltmann et al., 2020). Beam sensitive crystalline materials such as polymers can be investigated with 4D-STEM as well (Panova et al., 2019).

The success of DEDs to improve the resolution, sensitivity, flexibility, and efficiency of STEM experiments is truly creating a revolution in atomic- and nano-scale analysis on many fronts. Frame rate has been identified as a critical metric with the development of 1 bit operation and the introduction of event based detectors to significantly increase frame rate and reduce data rates (O'Leary et al., 2020; Plotkin-Swing et al., 2022; Stroppa et al., 2023). However, most current detectors operate with ~1–1.5 kHz acquisition rates, which is slower than typical STEM scanning rates of 100–1,000 kHz. This can lead to the incorporation of artifacts due to sample drift or charging (Jones et al., 2015; Ophus et al., 2016), especially in ptychography where phase information about the sample is found using the overlapping of adjacent probes. As an example, 1,024 by 1,024 probe positions is a common STEM scan size, and at 0.1–1 MHz scanning rate such an image can be acquired in under 30 s using an annular dark field (ADF) detector. A DED running at 1 kHz requires 17.5 min to acquire such a data set. Drift of the sample beyond the field-of-view is almost certain which indicates how faster detector acquisition is advantageous. Further, kHz acquisition rates also practically limits the achievable minimum dose applied to a sample, because the operator must reduce the beam current by a factor of 10–100 when switching from normal STEM imaging, which is used for focusing and aligning, to 4D-STEM in order to maintain the same dose (O'Leary et al., 2020). Further, slow acquisition rates limit the use of 4D-STEM for large field-of-view acquisitions and for complex STEM acquisition schemes such as focal series, electron

tomography, scan rotation series, *in situ*, and high throughput experiments. Recent successes have achieved excellent results at high frame rates at the cost of pixel binning. (Stroppa et al., 2023) The 4D Camera was designed to acquire full frame 4D-STEM data with a probe dwell time of 11 μs making 4D-STEM highly complementary to traditional STEM detectors. It excels in applications where speed is important such as atomic resolution imaging of materials and in relatively low and medium beam currents (~1–100 pA).

Materials and Methods

The 4D Camera sensor is mounted in a retractable Gatan K3 camera housing, making it immediately deployable on any TEM. It is currently installed on a double aberration-corrected Titan 80–300 named the TEAM 0.5 at the National Center for Electron Microscopy (NCEM) facility within the Molecular Foundry at Lawrence Berkeley National Laboratory. Each frame consists of 576 by 576 pixels digitized to 12 bits, which is about 4 Mbit per frame. At 87,000 Hz, the raw data rate is ~480 Gbit/s requiring a dedicated acquisition system to capture the full data rate. The full detector system (see Fig. 1) includes a set of field programmable gate arrays (FPGAs) for collecting and routing the digitized detector pixel signals and a set of computers for data capture, storage, and analysis. A 1/4 sector of each frame is handled separately by a dedicated FPGA/receiver pair during acquisition. The raw data are accumulated at the full rate into the memory of the four dedicated receiver servers over a high speed network consisting of 48 × 10 Gbit/s connections (12 links per receiver). After the STEM scan is complete, the data are then offloaded to flash memory installed in a fifth event builder server (named "Mothership 6") over 4 × 20 Gbit/s network connections.

The fifth server acts as the storage and processing computer for data reduction, postprocessing, and interactive analysis and is directly connected to the National Energy Research Computing Center (NERSC) by 100 Gbit fiber providing extra
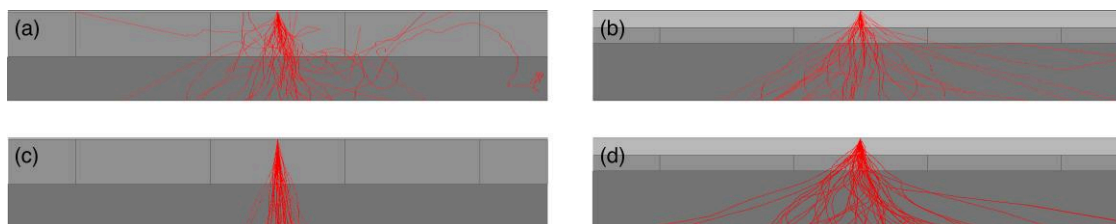
Fig. 2. Schematics of (**a,b**) 80 kV and (**c,d**) 300 kV electron scattering (red lines) in 10 μm wide APS pixels (vertical black lines). (**a**) and (**c**) show how a thinner inactive top layer (light gray) reduces electron scattering leading to reduced lateral energy deposition in the active layer (medium gray) compared to a sensor with a thicker inactive layer [(**b,d**)]. The active region is ~4–5 μm thick, and the thick inactive region in (**b**) and (**d**) is ~5 μm thick.

computational and storage capabilities for the large amounts of data generated. The open-source stempy (Avery et al., 2022) processing software was developed with Python, Numpy, and C++ to rapidly reduce the raw data by finding electron strikes. Other postprocessing such as center of mass (CoM) imaging is then accomplished using Jupyter notebooks applied directly to the sparse output data. The largest data size that can be acquired (due to memory limitations) is ~700 Gbytes (GB). The data reduction counting step can be accomplished locally using the fifth server in ~8 min or by multiple nodes on the NERSC super computing cluster in <5 min. Thus, the operator can receive rapid feedback at the microscope in typically <10 min to determine the quality of each scan even for these extremely large data sets. Rapid (even live) feedback to operators at the microscope has been identified as an important part of the future of electron microscopy allowing for data quality to be checked and results even generated during a microscope session (MacLaren et al., 2020; Spurgeon et al., 2021).

The sensor is a complementary metal oxide semiconductor (CMOS) active pixel sensor (APS) with 10 μm by 10 μm square pixels. APS sensors are designed to capture a few scattering events for each incident electron in the charge collection area while minimizing lateral charge deposition. See also Clough et al.'s review on the differences between different types of detectors (Clough & Kirkland, 2016). A schematic of such a CMOS sensor is shown in Figure 2 which demonstrates how front-side illuminated sensors with regions of material above the charge collection region broaden the range of energy deposition due to electron scattering. In general, front-side illuminated CMOS detectors are limited to operating at relatively high accelerating voltages (i.e., 300 kV) to minimize this effect and avoid damaging the chip electronics. The 4D Camera sensor was produced by thinning the inactive substrate layer to reduce electron scattering outside the active area. The sensor is back-side illuminated thus exposing the charge collection region first to the beam (see Figs. 2a and 2c). The detector was tested at accelerating voltages from 6 to 300 kV, and full charge deposition is seen at voltages below 30 kV. The sensor used to acquire the data in this manuscript was overthinned, removing some of the active region making it comparatively more sensitive with less lateral scattering at lower accelerating voltages.

For typical STEM experiments, the incident electron beam flux is sufficiently low, such that only about 1–2.5% of the detector pixels will be hit with an electron in each frame; however, it can also be used in "integration" mode where each pixel intensity is the sum of all charge deposited in a pixel allowing full frame movies to be acquired with high current. Here, we only discuss the detector for use in the sparse counting mode. During the design phase, we considered typical parameters for aberration-corrected STEM operating conditions (60–300 kV, ~10 μs dwell time, 1–100 pA beam current) in order to match 4D Camera operation as close as possible to normal operational parameters.

Using these parameters, 87,000 Hz was a chosen to match the ~10 μs dwell time used in typical HR-STEM image acquisitions. At such acquisition speeds and beam currents only about one electron will strike a pixel and the surrounding nearest- and second-nearest neighbors. The energy deposited in a pixel and the surrounding pixels is then used to determine the initial pixel location of the electron strike (Battaglia et al., 2009). The nature of electron scattering in a material dictates that the electron on average will deposit energy in a large surrounding area (Caswell et al., 2009), leading to PSF blurring. As shown in Figure 2, thinning the inactive layer and back-side illumination will reduce electron scattering, but the surrounding pixels can still have energy deposited in them. Further, the number of scattering events and amount of energy deposited is a stochastic process leading to a Landau distribution of energy deposition in each pixel (Denes et al., 2007). It is thus impractical to use the amount of energy captured in each pixel to differentiate the number of electrons. However, if the flux on the detector is sufficiently low (~50 pA), then we can assume with high confidence that only one electron will strike within any 3 by 3 pixel neighborhood creating a local peak. The pixel with the highest deposited energy is likely the original strike location of the electron, furthermore subpixel locations can be determined using centroiding (Li et al., 2013; Ruskin et al., 2013). In the simple case, the highest intensity pixel is counted as one electron regardless of energy deposition, and the surrounding pixels are set to zero which removes the PSF blurring. Coincidence loss (i.e., electrons hitting the same neighborhood) causes a ~5% counting error. This also leads to suppression of detector dark current noise and the ability to sum frames without adding detector noise (Battaglia et al., 2009). An added benefit is that the counted data are highly compressible leading to smaller storage and memory requirements and the ability to implement faster computation with algorithms designed to take advantage of this sparse data format (Pelz et al., 2022). What would be extremely large (>100 GB) datasets can be compressed 10--300× with the ability to fit in the working memory of consumer grade computers and graphical processing units (GPUs). The 4D Camera has been in operation since approximately Spring of 2019. The capabilities of the detector for several operating modes is presented and discussed in more detail below.

Results and Discussion

Typical STEM imaging experiments use radially symmetric, monolithic bright field (BF), annular BF, and/or ADF detectors to integrate electrons scattered to different angles in diffraction space. The choice of detectors and their inner/outer angles must be decided before an experiment is conducted. The use of a pixelated detector to capture the full scattering pattern provides the ability to generate traditional STEM image contrast with the
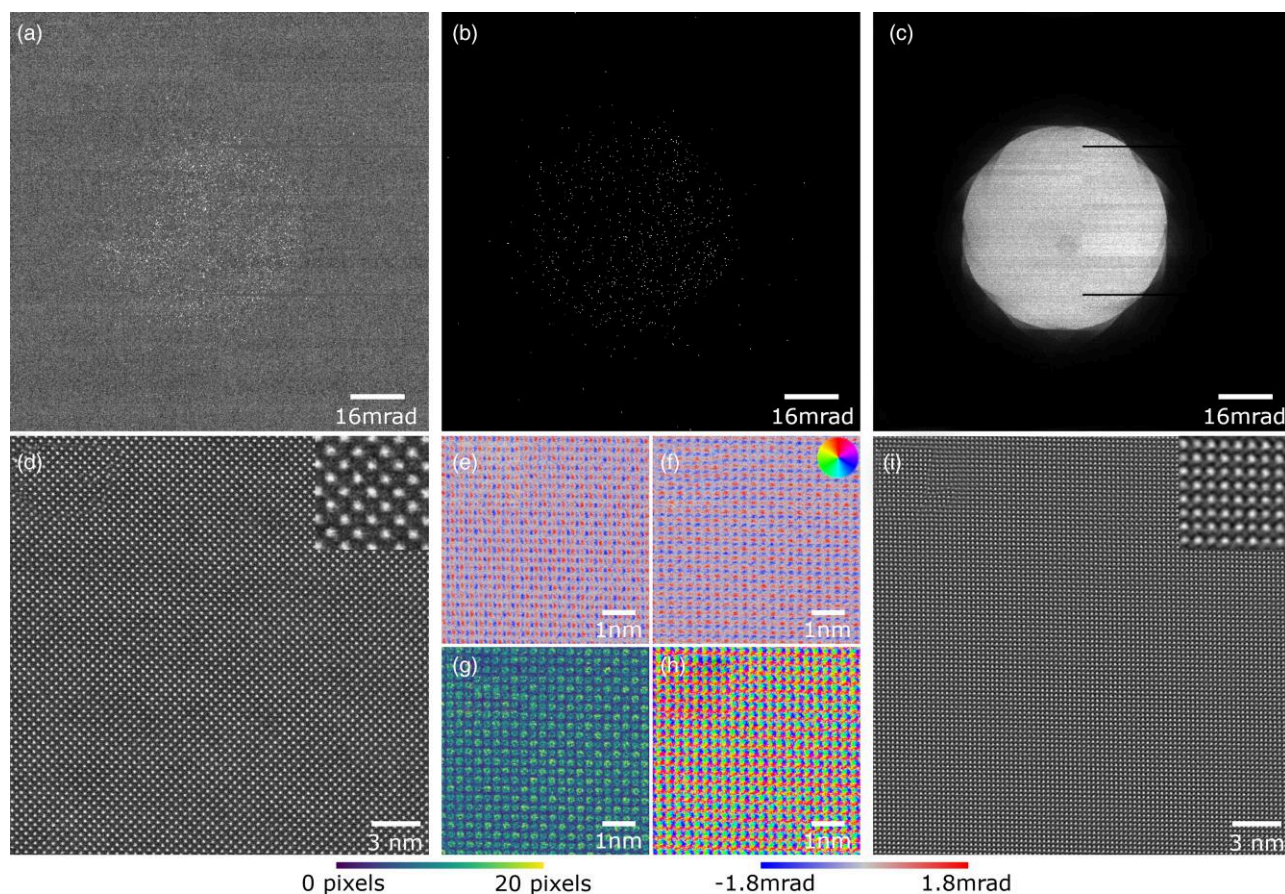
Fig. 3. High resolution STEM imaging of a $SrTiO_3/PbTiO_3$ multilayer. (**a**) A raw camera frame acquired in 11 μs from one scan position. (**b**) A single counted frame showing only electron strikes as bright pixels. (**c**) A PACBED pattern generated by summing the counted data. (**d**) The simultaneously acquired ADF-STEM image and magnified inlay. (**e–h**) The CoM_x, CoM_y, CoM_r, CoM_θ of a small 250 by 250 pixel region of the full scan. (**i**) The phase image calculated from the CoM_x and CoM_y with magnified inlay. The inlays have a field-of-view of 2.3 nm.

flexibility of choice as to the inner/outer angle(s) during postprocessing (MacLaren et al., 2020). The 4D Camera provides the ability to acquire a large, continuous range of scattering angles in the same amount of time as a typical STEM experiment (<15 s). Once electron counted, a radial sum algorithm implemented in the sparse domain (Avery et al., 2022; Pelz et al., 2022) further reduces the 4D data to 3D and allows a user to interactively set detector inner/outer angles for the desired STEM image contrast.

Figure 3 shows data acquired at high resolution from a highly converged electron beam of a $SrTiO_3(20)/PbTiO_3(20)/SrTiO_3(20)$ multilayer sample acquired perpendicular to the interfaces along the [100] direction. The sample was detached from a substrate and placed on a TEM grid using the process described in (Bakaul et al., 2016), and the nominal thickness was 23.64 nm. The STEM was operated at 300 kV with a convergence angle of 30 mrad and a beam current of about 50 pA. The thinned sensor is ~30% efficient at detecting 300 kV electrons, necessitating larger beam currents than should be necessary. Figure 3a shows a single raw camera frame. A faint outline of the central circular beam is visible but is obscured by camera dark noise. Figure 3b shows the same frame after it has been electron counted where each bright pixel indicates the location of one electron strike. Most electrons are within the central beam although some are scattered outside. Summation of all sparse frames from every scan position produces a position-averaged convergent beam electron diffraction (PACBED)

pattern, as shown in Figure 3c, which can be used to determine sample thickness, composition, and other properties (LeBeau et al., 2010; Ophus et al., 2017). Two dark horizontal rows are due to production defects in this first iteration of the detector, and other horizontal defects are due to nonlinear camera noise which are not removed due to the thin detector. Figure 3d shows the simultaneously acquired ADF-STEM image where the projected Pb and Ti/O columns show the expected Z-contrast.

The CoM was calculated for each counted frame in Figure 3. Even with the small number of electrons (see Fig. 3b) the CoM_x and CoM_y signal is quite strong as can be seen in the zoomed in Figures 3e and 3f, respectively. Atom positions are at the center of each red/blue blob. The radial deviation of the CoM (Fig. 3g) shows each atomic column with a singularity in the center as the beam passes directly over the column, and the vector angle is plotted in Figure 3h. Finally, the CoM images are used to calculate the phase signal resulting in Figure 3i over a 25.4 nm field of view with 0.025 nm real space pixel size. The pure oxygen columns are visible, but difficult to resolve at this length scale. Other datasets acquired with smaller probe step sizes clearly show the oxygen columns, but we display this medium magnification data set to demonstrate the ability to scan large regions for, e.g., polarization measurements (Yadav et al., 2016).

To show the capabilities of the detector for low-dose imaging of sensitive materials with high- and low-scattering elements, we chose a hexagonal $NaYF_4$ nanoparticle with core and shell doping of 15% thulium and 20% gadolinium,

respectively (Pedroso et al., 2021). These avalanching upconverting nanoparticles exhibit extremely large amplification factors due to a photo avalanche mechanism and are useful as probes in optical imaging of biological systems and high-density, rewritable 3D photopatterning (Lee et al., 2021, 2023). Several questions about the structure of these core/shell nanoparticles remain such as the dispersion of defects and dopants and the core/shell interface which could be answered by detailed high resolution analysis. The material is sensitive to the electron beam (Hobbs, 1973) and contains high- and low-scattering elements with small interatomic spacings difficult to resolve.

The nanoparticles are best imaged along the *c*-axis where mixing of atom species along the projection direction is minimized. Low-dose ADF-STEM measurements can resolve the yttrium atoms due to their relatively large Z-number, but the other atomic columns are weak scatterers. High resolution 4D-STEM scans were acquired using the 4D Camera with a 200 kV accelerating voltage, 17.1 mrad convergence angle, and each diffraction pattern contained ~150 electrons (2 pA beam current). 1,024 by 1,024 real space probe positions were required to image the entire 26 nm diameter nanoparticle in a 30 by 30 nm field of view with 0.029 nm pixel size with a total dose of ~1,800 $e^-/Å^2$. This allows the fluorine atomic columns to be resolved, while minimizing sample damage. The phase signal was extracted from CoM measurements of each diffraction pattern to produce the image shown in Figure 4. The inset shows the expected atomic arrangement overlaid on a magnified portion of the top edge of the nanoparticle where the hexagonal rings of the yttrium and 50/50 yttrium/sodium columns are seen as the brightest columns. At the center of each bright hexagon is a dimmer sodium column. Triangular arrangements of fluorine columns surround the brighter columns. In the center, some defects due to beam damage are seen, but the edge is fairly stable all around the nanoparticle. We found that the nanoparticle centers were more easily damaged by the beam which is either due to the thulium dopants
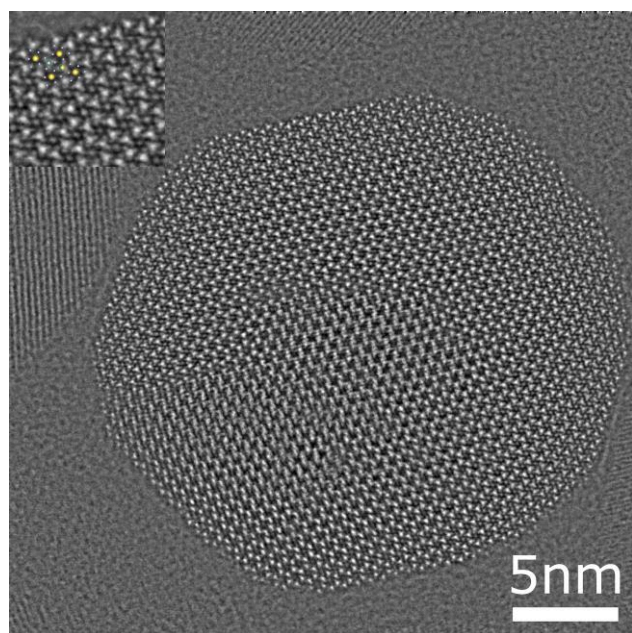

Fig. 4. Low-dose STEM phase imaging of a doped $NaYF_4$ nanoparticle. The inset shows a 4 nm by 4 nm magnified region of the edge of the nanoparticle where yttrium (medium green), sodium (large yellow), and fluorine (small white) atomic columns are visible.

in the core or more inelastic scattering due to the increase in projected thickness. The ability to simultaneously image high- and low-scattering elements in a large beam sensitive nanoparticle shows the capabilities of the 4D Camera for investigating new classes of materials previously too sensitive to image at high resolution using these techniques.

CoM is one type of phase contrast imaging that is relatively simple to extract from a pixelated detector. It does not, however, utilize the full range of information possible with such a detector and can be implemented using simple segmented detector with only four channels (Shibata et al., 2012; Bosch et al., 2016). A more advanced algorithm capable of using the entire scattering distribution is called ptychography (Humphry et al., 2012; Jiang et al., 2018). We implemented a ptychographic reconstruction method that takes advantage of the sparse nature of 4D Camera data providing large scale, rapid analysis on a modest GPU. The method is described in more detail in (Pelz et al., 2022) and is based on the single sideband (SSB) algorithm developed previously (Yang et al., 2015, 2017). In brief, the SSB ptychography method takes the Fourier transform of the 4D data hypercube along the probe scanning directions. Summation of the intensity within the double overlap regions of the double reciprocal space data set can then be used to determine the object function which approximates the projected potential of the sample in the weak scattering limit. The speed and sparse data output of the 4D Camera provides the ability to rapidly generate ptychographic reconstructions over a wide field-of-view in <10 min.

Figure 5 demonstrates the ptychographic reconstruction capabilities of the 4D Camera from a 1,024 by 1,024 4D-STEM scan with 0.03 nm real space pixel sampling of gold nanoparticles on an ultra-thin carbon substrate. The beam accelerating voltage was 80 kV, the convergence angle was 30 mrad, and the beam current was ~35 pA. At this accelerating voltage, the detector is ~50% efficient as measured by comparing the measured screen current from the Titan software to the flux of electron strikes incident on the detector. Figure 5a shows the virtual ADF-STEM image generated by summing all electron strikes within 46–72 mrad showing several ~5 nm gold nanoparticles. Figure 5b shows the phase image reconstruction using the same technique as used for Figures 3i and 4 where the atomic contrast is better resolved and more features are seen in the lightly scattering carbon substrate. Figure 5c shows the SSB ptychographic reconstruction from the same data set where more low frequencies and improved atomic contrast is evident with the inset Fourier transforms. Implementation of the SSB algorithm to take advantage of the sparse data output allows a 1,024 by 1,024 probe position 4D-STEM data set, which is originally 700 GB in raw form, to be processed by a GPU in <1 s (Pelz et al., 2022). The three images are calculated from the same data set.

Another common experimental mode of 4D-STEM is nanobeam electron diffraction (NBED), where the convergence angle of the STEM probe is reduced to avoid overlap of diffracted beams on the detector (Ophus, 2019). The probe is localized to approximately the nanometer scale and can provide information about crystal phase, orientation, and strain while also providing the ability to generate virtual BF and virtual ADF real space images from any desired scattering angles. The speed of the 4D Camera provides the ability to scan over very large fields-of-view reducing the need to carefully choose the region of interest. Full devices or a battery stack can be rapidly investigated with nanometer scale real space pixel sizes over a tens of micron-sized field of view. The concentrated intensity of intense Bragg spots can lead to undercounting in
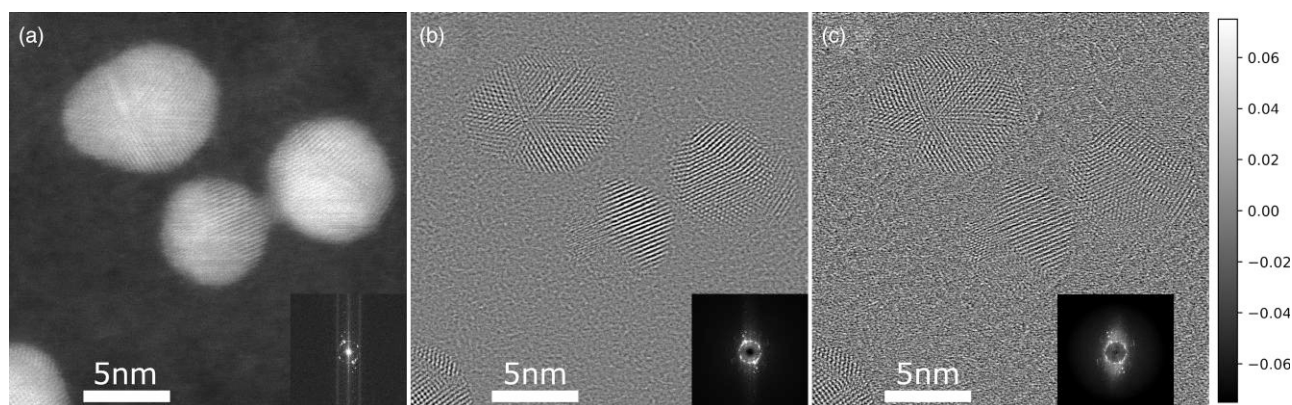
Fig. 5. Phase contrast STEM imaging of gold nanoparticles on carbon. (**a**) ADF-STEM image generated from the sparse 4D data set. (**b**) Phase image from CoM created from the sparse 4D data set. (**c**) The phase calculated by single side band ptychographic processing from the sparse data set. Color bar represents radian phase shift in (**c**). All images were generated from the same data set.

some cases. The position of the Bragg peak is well represented, but intensity is lower than expected.

The ability of the detector to investigate an entire device was tested on a focused ion beam (FIB) liftout of a 15 by 15 μm sized battery stack composed of (from top to bottom) platinum and aluminum protective layers, titanium, LiPON, LiCoO$_2$, nickel, aluminum, and silicon as shown in the overview scanning electron microscopy (SEM) image of the entire FIB liftout seen in Figure 6b. The region scanned by 4D-STEM presented in Figures 6a and 6c is indicated as a red box on the SEM image of the FIB liftout in Figure 6b. The thickness of each region of the battery stack can be differentiated by Z-contrast in the ADF-STEM image in Figure 6c simultaneously acquired with the 4D-STEM data.

The 4D Camera was used to acquire several separate scans of the thin area of the specimen with 256 by 1,024 real space probe positions to improve the signal to noise. In total ten frames were acquired per probe position with a total acquisition time of 38 s. The rapidity of the scans and the nanometer scale scanning step size meant that sample drift could be ignored. The microscope was operated at 300 kV and configured in a nearly parallel beam configuration with a convergence angle of about 1 mrad. A patterned aperture was used to improve the ability to localize individual diffraction spots (Zeltmann et al., 2020). The beam was rastered with a step size of 12.8 nm over a field-of-view of 3.27 μm by 13.07 μm. Each scan was reduced to electron counts, and the shifts of the electron beam on the detector due to scanning a large field of view were removed using shifts from a vacuum scan acquired at the same STEM magnification and camera length. The reduced, combined data set (originally 1,740 GB of raw data) only required 3.8 GB of disk space in the sparse format.

A tiled visualization of a small subset of the 4D-STEM data is shown in Figure 6a along with the simultaneously acquired ADF-STEM image from only the first scan (Fig. 6c). To fit the page, only one in sixteen patterns is displayed, and each diffraction pattern is binned by eight to 72 by 72 pixels. The regions of interest (ROIs) enclosed in blue, orange, and green boxes are enlarged to show more detail. Figure 6d is from the blue rectangle where the LiPON directly contacts the LiCoO$_2$ for the

electrolyte–electrode interface. The diffraction patterns at the top of Figure 6d do not show any spots indicating the LiPON is amorphous. The orange ROI enlarged in Figure 6e is from a thin LiCoO$_2$ region and shows that diffraction patterns along the vertical direction are more similar as compared to their horizontal neighbors indicating grains are extended vertically along the growth direction (columnar growth). The patterns in the green rectangle (Fig. 6f) are from the LiCoO$_2$/nickel/aluminum interfaces at the bottom electrode. Differences in crystal orientation and structure are clearly visible, but require advanced processing for quantitative understanding of such a large data set beyond the scope of this demonstration (Rauch & Dupuy, 2005; Brunetti et al., 2011; Savitzky et al., 2021; Ophus et al., 2022).

Figure 6g is the sum of every pattern in the full data set showing several distinct rings as well as the shape of the patterned aperture. Interestingly, the inner-most ring is brighter on the top and bottom compared to the horizontal direction which matches the real space horizontal–vertical scanning directions. This supports a preferential direction for the LiCoO$_2$ crystals visually identified in Figure 6e. Summation of intensity for a range of scattering angles for rings of interest produces the virtual ADF-STEM images shown in Figure 7. The images correspond to scattering from the LiCo$_2$ (a) [111], (b) [311] and [222], (c) [400], and (d) [440] family of reflections (Wang et al., 1999; Kushida & Kuriyama, 2002). Such vertical grain growth is shown in higher detail using a zoomed in portion of the upper left region of the full scan as shown in Figure 8a. The sum of all diffraction patterns from this region is shown in Figure 8c which has arcs rather than full rings indicating a preferential direction for many grains. Colored boxes for the different parts of an arc indicate where the red, green, and blue contrast is generated in Figure 8b. The vertical grain texture is apparent and adjacent grains are related by a small in-plane rotation.

Solid state battery degradation and failure are directly linked to the electrochemical and mechanical limitations of bulk electrode, electrolyte material layers and their interfaces (Tan et al., 2020). Data acquisition at this scale and rapidity provides bulk and localized, granular structural information of the solid state battery system that can be used to highlight crystallographic preferences within bulk
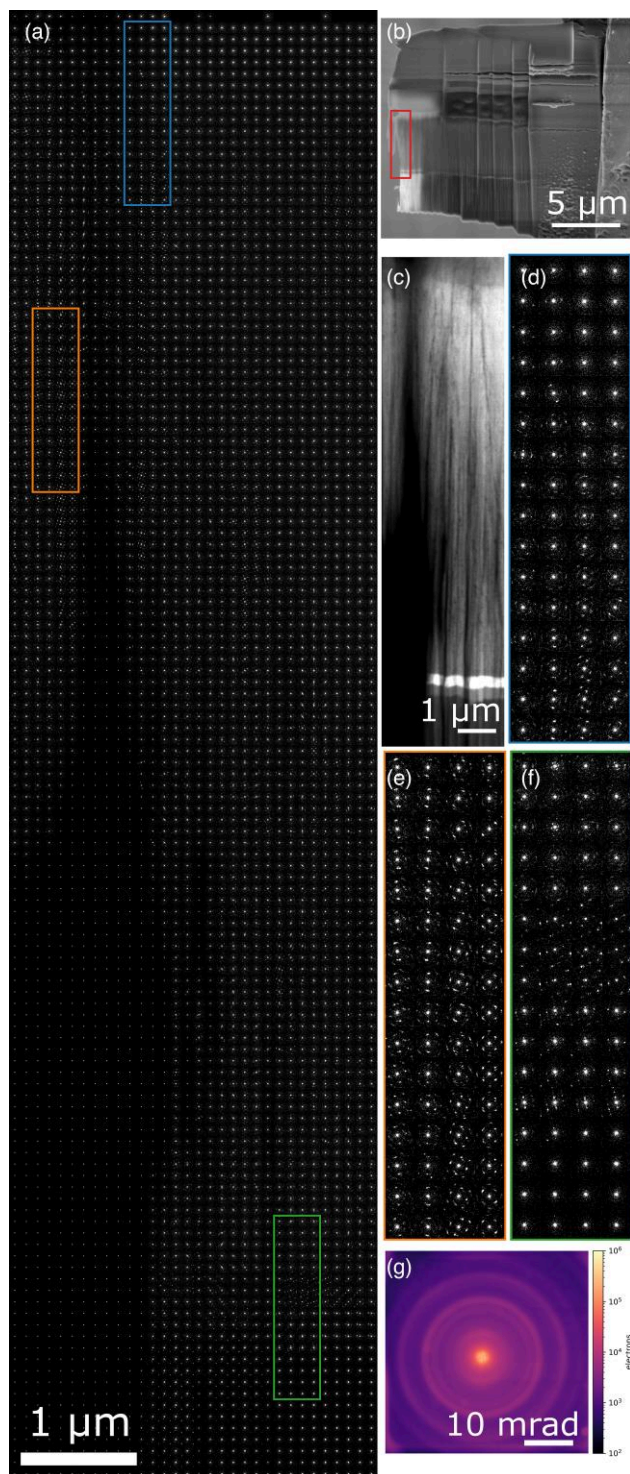
Fig. 6. Large-scale near-parallel beam 4D-STEM scan of a battery stack. (**a**) A subset of diffraction patterns tiled next to each other representing 1/16th of the probe positions in each direction. The diffraction patterns are binned by eight to fit the page. (**b**) An overview image of the full FIB liftout sample. The region presented in (**a**) and (**c**) is indicated by a rectangle (red). (**c**) The simultaneously acquired ADF-STEM image for one 4D-STEM scan showing the full battery stack with Z-contrast. The regions in the (**d**) top blue, (**e**) left orange, and (**f**) bottom green boxes shown in (**a**) are enlarged to show the details of the diffraction patterns for different regions of interest. (**g**) The sum of all diffraction patterns overlaid with the radial sum of all diffraction patterns showing several diffraction rings. The colorbar is in units of electrons and on a log scale.
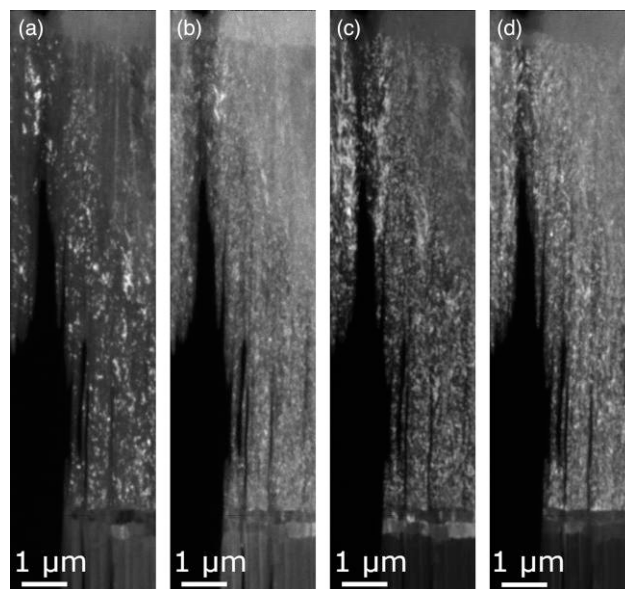
Fig. 7. Virtual ADF-STEM images generated using a rotational sum for each diffraction pattern. Refer to Figure 6g to see each ring in the full data set. The images are generated using scattering from the (**a**) [111], (**b**) [311] and [222], (**c**) [400], and (**d**) [440] family of reflections in $LiCO_2$.

$LiCoO_2$, modifications in structure of $LiCoO_2$ from electrode bulk to electrode–electrolyte interface, as well as other structural patterns. This data, if combined with complementary EELS information, can develop a statistically robust analysis of initial microstructure, charge–discharge microstructure evolution as affected by lithium ion movement, and finally, breakdown of lithium ion transport, i.e. battery failure.

Summary

The 4D Camera's high frame rate and data rate enable rapid scanning with the possibility to integrate 4D-STEM into complex experiments and modalities. The integration of the camera with large computational resources reduces feedback time to the operator from days to minutes. The 4D Camera allows a STEM to be treated as a multifunctional electron scattering beamline which goes beyond the traditional "single image acquisition" approach in favor of capturing all scattering information where one can effectively perform many experiments on a single, large multidimensional data set with massive data analytics. The next iteration of the detector chip at NCEM will be thicker to increase the signal to noise. A streaming-based data workflow is being developed to avoid costly file writing operations to improve throughput. A second 4D Camera system is currently being commissioned at a second site. Also, a newly designed detector is being readied specifically for EELS which includes variable pixel readout rates across the chip to allow counting of the high intensity zero loss peak.

Availability of Data and Materials

The authors have declared that no datasets apply for this piece.
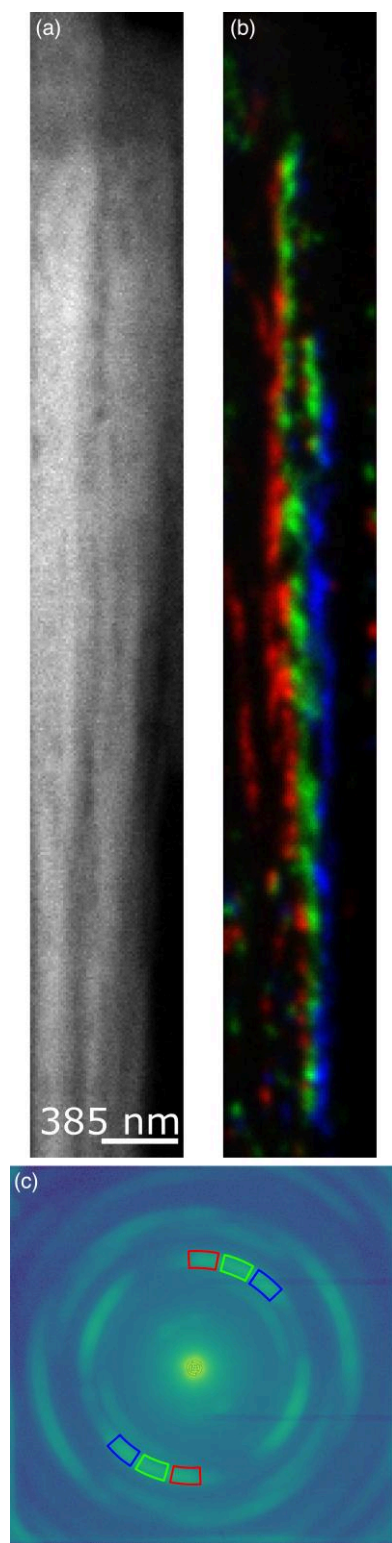
Fig. 8. Vertical grains. (**a**) The zoomed in portion of the ADF-STEM image of the upper left corner of Figure 6c. (**b**) A red–green–blue composite image of three virtual ADF images generated from the colored boxes indicated in the diffraction pattern in (**c**). (**c**) The summed diffraction pattern with colored boxes indicating the masks used to generate (**b**).

Acknowledgements

Financial Support

Conflict of Interest

The authors declare that they have no competing interest.

References

Avery P, Harris C, Ercius P, Genova A, Hanwell MD & Zhao Z (2022). OpenChemistry/stempy: stempy 3.2.0. https://doi.org/10.5281/zenodo.7083493

Bakaul SR, Serrao CR, Lee M, Yeung CW, Sarker A, Hsu S-L, Yadav AK, Dedon L, You L, Khan AI, Clarkson JD, Hu C, Ramesh R & Salahuddin S (2016). Single crystal functional oxides on silicon. *Nat Commun* **7**(1), 10547. https://doi.org/10.1038/ncomms10547

Battaglia M, Contarato D, Denes P & Giubilato P (2009). Cluster imaging with a direct detection CMOS pixel sensor in transmission electron microscopy. *Nucl Instrum Methods Phys Res Sec A: Accel Spectrom Detect Assoc Equip* **608**(2), 363–365. https://doi.org/10.1016/j.nima.2009.07.017

Bosch EGT, Lazic I & Lazar S (2016). Integrated differential phase contrast (iDPC) STEM: A new atomic resolution STEM technique to image all elements across the periodic table. *Microsc Microanal* **22**, 306–307. https://doi.org/10.1017/S1431927616002385

Brilot AF, Chen JZ, Cheng A, Pan J, Harrison SC, Potter CS, Carragher B, Henderson R & Grigorieff N (2012). Beam-induced motion of vitrified specimen on holey carbon film. *J Struct Biol* **177**(3), 630–637. https://doi.org/10.1016/j.jsb.2012.02.003

Brown H, Chen Z, Weyland M, Ophus C, Ciston J, Allen L & Findlay S (2018). Structure retrieval at atomic resolution in the presence of multiple scattering of the electron probe. *Phys Rev Lett* **121**(26), 266102. https://doi.org/10.1103/PhysRevLett.121.266102

Brown HG, Pelz PM, Hsu S-L, Zhang Z, Ramesh R, Inzani K, Sheridan E, Griffin SM, Schloz M, Pekin TC, Koch CT, Findlay SD, Allen LJ, Scott MC, Ophus C & Ciston J (2022). A three-dimensional reconstruction algorithm for scanning transmission electron microscopy data from a single sample orientation. *Microsc Microanal* **28**(5), 1632–1640. https://doi.org/10.1017/S1431927622012090

Brunetti G, Robert D, Bayle-Guillemaud P, Rouvière JL, Rauch EF, Martin JF, Colin JF, Bertin F & Cayron C (2011). Confirmation of the domino-cascade model by LiFePO4/FePO4 precession electron diffraction. *Chem Mater* **23**(20), 4515–4524. https://doi.org/10.1021/cm201783z

Caswell T, Ercius P, Tate M, Ercan A, Gruner S & Muller D (2009). A high-speed area detector for novel imaging techniques in a scanning transmission electron microscope. *Ultramicroscopy* **109**(4), 304–311. https://doi.org/10.1016/j.ultramic.2008.11.023

Chen Z, Jiang Y, Shao Y-T, Holtz ME, Odstrcil M, Guizar-Sicairos M, Hanke I, Ganschow S, Schlom DG & Muller DA (2021). Electron ptychography achieves atomic-resolution limits set by lattice vibrations. *Science* **372**(6544), 826–831. https://doi.org/10.1126/science.abg2533

Clough R & Kirkland AI (2016). Direct Digital Electron Detectors. In *Advances in Imaging and Electron Physics*, Hawkes Peter W. (Eds.), pp. 1–42, vol. 198. Elsevier.

Denes P, Bussat J-M, Lee Z & Radmillovic V (2007). Active pixel sensors for electron microscopy. *Nucl Instrum Methods Phys Res Sec A: Accel Spectrom Detect Assoc Equip* **579**(2), 891–894. https://doi.org/10.1016/j.nima.2007.05.308

Grob P, Bean D, Typke D, Li X, Nogales E & Glaeser RM (2013). Ranking TEM cameras by their response to electron shot noise. *Ultramicroscopy* **133**, 1–7. https://doi.org/10.1016/j.ultramic.2013.01.003

Hachtel JA, Idrobo JC & Chi M (2018). Sub-Ångstrom electric field measurements on a universal detector in a scanning transmission electron microscope. *Adv Struct Chem Imaging* **4**(1), 10. https://doi.org/10.1186/s40679-018-0059-4

Hart JL, Lang AC, Leff AC, Longo P, Trevor C, Twesten RD & Taheri ML (2017). Direct detection electron energy-loss spectroscopy: A method to push the limits of resolution and sensitivity. *Sci Rep* **7**(1), 8243. https://doi.org/10.1038/s41598-017-07709-4

Hirata A, Guan P, Fujita T, Hirotsu Y, Inoue A, Yavari AR, Sakurai T & Chen M (2011). Direct observation of local atomic order in a metallic glass. *Nat Mater* **10**(1), 28–33. https://doi.org/10.1038/nmat2897

Hobbs LW (1973). Transmission electron microscopy of defects in alkali halides. *J Phys Colloque* **34**(C9), 227–241. https://doi.org/10.1051/jphyscol:1973941

Humphry MJ, Kraus B, Hurst AC, Maiden AM & Rodenburg JM (2012). Ptychographic electron microscopy using high-angle dark-field scattering for sub-nanometre resolution imaging. *Nat Commun* **3**(1), 730. https://doi.org/10.1038/ncomms1733

Jiang Y, Chen Z, Han Y, Deb P, Gao H, Xie S, Purohit P, Tate MW, Park J, Gruner SM, Elser V & Muller DA (2018). Electron ptychography of 2D materials to deep sub-ångström resolution. *Nature* **559**(7714), 343–349. https://doi.org/10.1038/s41586-018-0298-5

Jones L, Yang H, Pennycook TJ, Marshall MSJ, Van Aert S, Browning ND, Castell MR & Nellist PD (2015). Smart align—a new tool for robust non-rigid registration of scanning microscope data. *Adv Struct Chem Imaging* **1**(1), 1–16. https://doi.org/10.1186/s40679-015-0008-4

Kim BH, Heo J, Kim S, Reboul CF, Chun H, Kang D, Bae H, Hyun H, Lim J, Lee H, Han B, Hyeon T, Alivisatos AP, Ercius P, Elmlund H & Park J (2020). Critical differences in 3D atomic structure of individual ligand-protected nanocrystals in solution. *Science* **368**(6486), 60–67. https://doi.org/10.1126/science.aax3233

Kushida K & Kuriyama K (2002). Narrowing of the co-3d band related to the order–disorder phase transition in LiCoO2. *Solid State Commun* **123**(8), 349–352. https://doi.org/10.1016/S0038-1098(02)00325-3

LeBeau JM, Findlay SD, Allen LJ & Stemmer S (2010). Position averaged convergent beam electron diffraction: Theory and applications. *Ultramicroscopy* **110**(2), 118–125. https://doi.org/10.1016/j.ultramic.2009.10.001

Lee C, Xu EZ, Kwock KWC, Teitelboim A, Liu Y, Park HS, Ursprung B, Ziffer ME, Karube Y, Fardian-Melamed N, Pedroso CCS, Kim J, Pritzl SD, Nam SH, Lohmueller T, Owen JS, Ercius P, Suh YD, Cohen BE, Chan EM & Schuck PJ (2023). Indefinite and bidirectional near-infrared nanocrystal photoswitching. *Nature* **618**(7967), 951–958. https://doi.org/10.1038/s41586-023-06076-7

Lee C, Xu EZ, Liu Y, Teitelboim A, Yao K, Fernandez-Bravo A, Kotulska AM, Nam SH, Suh YD, Bednarkiewicz A, Cohen BE, Chan EM & Schuck PJ (2021). Giant nonlinear optical responses from photon-avalanching nanoparticles. *Nature* **589**(7841), 230–235. https://doi.org/10.1038/s41586-020-03092-9

Li X, Zheng SQ, Egami K, Agard DA & Cheng Y (2013). Influence of electron dose rate on electron counting images recorded with the K2 camera. *J Struct Biol* **184**(2), 251–260. https://doi.org/10.1016/j.jsb.2013.08.005

MacLaren I, Macgregor TA, Allen CS & Kirkland AI (2020). Detectors—the ongoing revolution in scanning transmission electron microscopy and why this important to material characterization. *APL Mater* **8**(11), 110901. https://doi.org/10.1063/5.0026992

McMullan G, Chen S, Henderson R & Faruqi AR (2009). Detective quantum efficiency of electron area detectors in electron microscopy. *Ultramicroscopy* **109**(9), 1126–1143. https://doi.org/10.1016/j.ultramic.2009.04.002

Murthy AA, Ribet SM, Stanev TK, Liu P, Watanabe K, Taniguchi T, Stern NP, Reis RD & Dravid VP (2021). Spatial mapping of electrostatic fields in 2D heterostructures. *Nano Lett* **21**(17), 7131–7137. https://doi.org/10.1021/acs.nanolett.1c01636

Nord M, Webster RWH, Paton KA, McVitie S, McGrouther D, MacLaren I & Paterson GW (2020). Fast pixelated detectors in scanning transmission electron microscopy. Part I: Data acquisition, live processing, and storage. *Microsc Microanal* **26**(4), 653–666. https://doi.org/10.1017/S1431927620001713

O'Leary CM, Allen CS, Huang C, Kim JS, Liberti E, Nellist PD & Kirkland AI (2020). Phase reconstruction using fast binary 4D STEM data. *Appl Phys Lett* **116**(12), 124101. https://doi.org/10.1063/1.5143213

Ophus C (2019). Four-dimensional scanning transmission electron microscopy (4D-STEM): From scanning nanodiffraction to ptychography and beyond. *Microsc Microanal* **25**(3), 563–582. https://doi.org/10.1017/S1431927619000497

Ophus C, Ciston J & Nelson CT (2016). Correcting nonlinear drift distortion of scanning probe and scanning transmission electron microscopies from image pairs with orthogonal scan directions. *Ultramicroscopy* **162**, 1–9. https://doi.org/10.1016/j.ultramic.2015.12.002

Ophus C, Ercius P, Huijben M & Ciston J (2017). Non-spectroscopic composition measurements of SrTio3-La0. 7Sr0. 3MnO3 multi-layers using scanning convergent beam electron diffraction. *Appl Phys Lett* **110**(6), 063102. https://doi.org/10.1063/1.4975932

Ophus C, Zeltmann SE, Bruefach A, Rakowski A, Savitzky BH, Minor AM & Scott MC (2022). Automated crystal orientation mapping in py4DSTEM using sparse correlation matching. *Microsc Microanal* **28**(2), 1–14. https://doi.org/10.1017/S1431927622000101

Ozdol VB, Gammer C, Jin XG, Ercius P, Ophus C, Ciston J & Minor AM (2015). Strain mapping at nanometer resolution using advanced nano-beam electron diffraction. *Appl Phys Lett* **106**(25), 253107. https://doi.org/10.1063/1.4922994

Panova O, Ophus C, Takacs CJ, Bustillo KC, Balhorn L, Salleo A, Balsara N & Minor AM (2019). Diffraction imaging of nanocrystalline structures in organic semiconductor molecular thin films. *Nat Mater* **18**(8), 860–865. https://doi.org/10.1038/s41563-019-0387-3

Park J, Elmlund H, Ercius P, Yuk JM, Limmer DT, Chen Q, Kim K, Han SH, Weitz DA, Zettl A & Alivisatos AP (2015). 3D structure of individual nanocrystals in solution by electron microscopy. *Science* **349**(6245), 290–295. https://doi.org/10.1126/science.aab1343

Paterson GW, Webster RW, Ross A, Paton KA, Macgregor TA, McGrouther D, MacLaren I & Nord M (2020). Fast pixelated detectors in scanning transmission electron microscopy. Part ii: Post-acquisition data processing, visualization, and structural characterization. *Microsc Microanal* **26**(5), 944–963. https://doi.org/10.1017/S1431927620024307

Pedroso CCS, Mann VR, Zuberbuhler K, Bohn M-F, Yu J, Altoe V, Craik CS & Cohen BE (2021). Immunotargeting of nanocrystals by SpyCatcher conjugation of engineered antibodies. *ACS Nano* **15**(11), 18374–18384. https://doi.org/10.1021/acsnano.1c07856

Pelz PM, Johnson I, Ophus C, Ercius P & Scott MC (2022). Real-time interactive 4d-STEM phase-contrast imaging from electron event representation data: Less computation with the right representation. *IEEE Signal Process Mag* **39**(1), 25–31. https://doi.org/10.1109/MSP.2021.3120981

Plotkin-Swing B, Haas B, Mittelberger A, Dellby N, Hotz M, Hrncirik P, Meyer C, Zambon P, Hoermann C, Meffert M, Bachevskaya D, Piazza L, Krivanek OL & Lovejoy TC (2022). 100,000 diffraction patterns per second with live processing for 4D-STEM. *Microsc Microanal* **28**(S1), 422–424. https://doi.org/10.1017/S1431927622002392
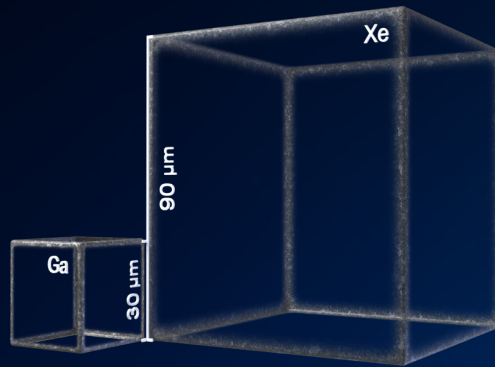
Rauch EF & Dupuy L (2005). Rapid spot diffraction patterns idenfification through template matching. *Arch Metall Mater* **50**(1), 87–99.

Ruskin RS, Yu Z & Grigorieff N (2013). Quantitative characterization of electron detectors for transmission electron microscopy. *J Struct Biol* **184**(3), 385–393. https://doi.org/10.1016/j.jsb.2013.10.016

Savitzky BH, Zeltmann SE, Hughes LA, Brown HG, Zhao S, Pelz PM, Pekin TC, Barnard ES, Donohue J, Rangel DaCosta L, Kennedy E, Xie Y, Janish MT, Schneider MM, Herring P, Gopal C, Anapolsky A, Dhall R, Bustillo KC, Ercius P, Scott MC, Ciston J, Minor AM & Ophus C (2021). py4dstem: A software package for four-dimensional scanning transmission electron microscopy data analysis. *Microsc Microanal* **27**(4), 712–743. https://doi.org/10.1017/S1431927621000477

Shibata N, Findlay SD, Kohno Y, Sawada H, Kondo Y & Ikuhara Y (2012). Differential phase-contrast microscopy at atomic resolution. *Nat Phys* **8**(8), 611–615. https://doi.org/10.1038/nphys2337

Spurgeon SR, Ophus C, Jones L, Petford-Long A, Kalinin SV, Olszta MJ, Dunin-Borkowski RE, Salmon N, Hattar K, Yang W-CD, Sharma R, Du Y, Chiaramonti A, Zheng H, Buck EC, Kovarik L, Penn RL, Li D, Zhang X, Murayama M & Taheri ML (2021). Towards data-driven next-generation transmission electron microscopy. *Nat Mater* **20**(3), 274–279. https://doi.org/10.1038/s41563-020-00833-z

Stroppa DG, Meffert M, Hoermann C, Zambon P, Bachevskaya D, Remigy H, Schulze-Briese C & Piazza L (2023). From STEM to 4D STEM: Ultrafast diffraction mapping with a hybrid-pixel detector. *Micros Today* **31**(2), 10–14. https://doi.org/10.1093/mictod/qaad005

Susarla S, Naik MH, Blach DD, Zipfel J, Taniguchi T, Watanabe K, Huang L, Ramesh R, da Jornada FH, Louie SG, Ercius P & Raja A (2022). Hyperspectral imaging of exciton confinement within a moiré unit cell with a subnanometer electron probe. *Science* **378**(6625), 1235–1239. https://doi.org/10.1126/science.add9294

Tan DHS, Banerjee A, Chen Z & Meng YS (2020). From nanoscale interface characterization to sustainable energy storage using all-solid-state batteries. *Nat Nanotechnol* **15**(3), 170–180. https://doi.org/10.1038/s41565-020-0657-x

Wang H, Jang Y, Huang B, Sadoway DR & Chiang Y (1999). TEM study of electrochemical cycling-induced damage and disorder in LiCoO2 cathodes for rechargeable lithium batteries. *J Electrochem Soc* **146**(2), 473–480. https://doi.org/10.1149/1.1391631

Yadav AK, Nelson CT, Hsu SL, Hong Z, Clarkson JD, Schlepütz CM, Damodaran AR, Shafer P, Arenholz E, Dedon LR, Chen D, Vishwanath A, Minor AM, Chen LQ, Scott JF, Martin LW & Ramesh R (2016). Observation of polar vortices in oxide superlattices. *Nature* **530**(7589), 198–201. https://doi.org/10.1038/nature16463

Yang H, MacLaren I, Jones L, Martinez GT, Simson M, Huth M, Ryll H, Soltau H, Sagawa R, Kondo Y, Ophus C, Ercius P, Jin L, Kovacs A & Nellist PD (2017). Electron ptychographic phase imaging of light elements in crystalline materials using Wigner distribution deconvolution. *Ultramicroscopy* **180**, 173–179. https://doi.org/10.1016/j.ultramic.2017.02.006

Yang H, Pennycook TJ & Nellist PD (2015). Efficient phase contrast imaging in STEM using a pixelated detector. Part II: Optimisation of imaging conditions. *Ultramicroscopy* **151**, 232–239. https://doi.org/10.1016/j.ultramic.2014.10.013

Zeltmann SE, Müller A, Bustillo KC, Savitzky B, Hughes L, Minor AM & Ophus C (2020). Patterned probes for high precision 4D-STEM bragg measurements. *Ultramicroscopy* **209**, 112890. https://doi.o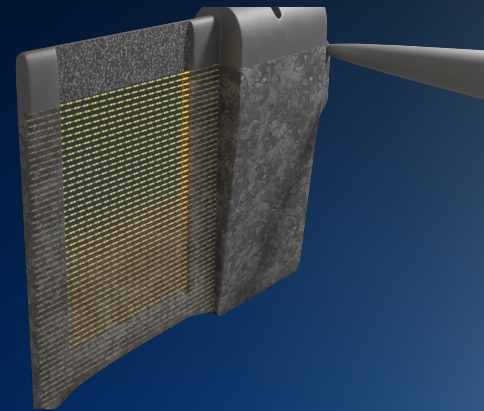rg/10.1016/j.ultramic.2019.112890